

# Nonadiabaticity under compression in metastable carbon monoxide-nitroxide mixtures

Reetam Paul,<sup>1</sup> Jonathan C. Crowhurst,<sup>1</sup> and Stanimir A. Bonev<sup>1</sup>

<sup>1</sup>Lawrence Livermore National Laboratory, 7000 East Avenue, Livermore, CA 94550

Carbon monoxide (CO) and nitrous oxide (N<sub>2</sub>O) both undergo profound structural and chemical transformations when compressed. While their individual high-*P/T* phase diagrams have been mapped in considerable detail, comparatively little attention has been paid to the *mixtures* in which the two species can couple through oxygen transfer, charge redistribution, and nonadiabatic dissociation pathways. Here we use comprehensive *ab initio* adiabatic/nonadiabatic molecular dynamics simulations, essentially a *diabatic trajectory stitching* approach, that chart the evolution of CO–N<sub>2</sub>O mixtures from van-der-Waals fluids to extended amorphous network solids over the range 0–160 GPa and 300–1500 K. We emphasize on (i) the sequence of gas → molecular crystal → polymerized amorphous solid reactive transitions that arise from an interplay between thermal and compression effects in metastable C–N–O mixtures, (ii) the role of N<sub>2</sub>O unimolecular dissociation in lowering the onset pressure for CO polymerization, and (iii) the emergence of nonadiabatic pathways, via thermal unimolecular dissociation of N<sub>2</sub>O, accompanied by spin-transition in oxygen atoms that can make C–N–O systems deviate from Born–Oppenheimer dynamics. This dominates the chemistry once the mixture enters the regime of bond-breaking temperatures (*T*  $\gtrsim$  900 K).

PACS numbers:

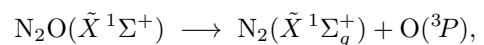
Energetic materials store large amounts of chemical energy in the form of strained or highly polarized bonds [1], releasing a large fraction of that energy when those bonds relax to lower-energy configurations [2, 3]. One route to such states is the high-energy-density (HED) route of pressure-induced polymerization of small, stable molecules into extended networks in which every atom sits in an energetically *over-bonded* environment [4–6]. Because such transformations are driven by extreme compression and often high temperatures, the resulting frameworks can trap a substantial portion of the compression (*PV*) work done on them; if the phase can be metastably quenched and recovered to ambient conditions, that stored mechanical work becomes latent chemical energy. These high-pressure amorphous or disordered structures – often lacking long-range crystalline order yet comprising robust covalent networks – can potentially be used as energy-dense carbonaceous poly-nitro oxidizers [7]. Two extensively researched examples illustrate this concept. Compressed carbon dioxide phase V (CO<sub>2</sub>-V), which forms above 60 GPa [8], where molecular CO<sub>2</sub> polymerizes into a three-dimensional, four-coordinated, diamond-like sp<sup>3</sup> C–O framework analogous to silica; on rapid decompression to ambient pressure it can survive below 185 K [8]. Likewise, cubic gauche nitrogen (*cg*-N) – synthesized near 110 GPa and >2000 K – locks every nitrogen into single, gauche-conformed N–N bonds, trapping the  $\sim$ 781 kJ/mol enthalpic penalty of delocalizing the triple bonds of N<sub>2</sub> [4]. Although both cases require diamond anvil cell conditions for synthesis and have prohibitive kinetic barriers and/or limited ambient recoverability [9, 10], they demonstrate how high-pressure amorphous or disordered solids could underwrite a new class of super-energetic materials once scalable routes to metastable recovery are developed.

This led us to investigate mixtures which are funda-

mentally C–N–O based but built using metastable mixtures of carbon monoxide (CO) and nitroxides (in this case, nitrous oxide N<sub>2</sub>O). The expectation was that these might be more energetic and recoverable relative to the baseline stable molecular cases of CO<sub>2</sub> and N<sub>2</sub>. Stoichiometrically, such a mixture is equivalent to an equimolar mixture of molecular CO<sub>2</sub> and N<sub>2</sub>.

CO polymerizes above *P*  $\simeq$  5–10 GPa to a Pa $\bar{3}$  cubic lattice at 300 K, forming layered sp<sup>2</sup>–sp<sup>3</sup> carbon–oxygen frameworks with energy densities rivaling energetic polymers and certain nitramines. Above that, infrared and X-ray [11] signatures of  $\pi$ -bond collapse appear, signalling the formation of a lactone-type polymer [6]; the product densifies smoothly to  $\rho \approx 2.6 \text{ g cm}^{-3}$  by 40 GPa. Recent *ab initio* structure searches revealed even denser layered polymorphs (Cmcm, *P2*<sub>1</sub>/*c*) that become more stable than previously proposed chains beyond 90 GPa [13, 14].

N<sub>2</sub>O, in contrast, remains molecular till much higher pressures; remaining linear and centrosymmetric much further: Phase I (Pa $\bar{3}$ ) persists to 10 GPa [15], Phase II (bent, *C2/m*) appears at  $\sim$  12 GPa [15], and the fully bent *Pbcn* Phase IV is accessed only above 18 GPa and 600 K [16], before ultimately undergoing heterolytic disproportionation into NO<sup>+</sup>NO<sub>3</sub><sup>–</sup> and N<sub>2</sub> [17]. The key divergence, at high pressures, from the CO<sub>2</sub> analogy is that bent N<sub>2</sub>O eventually *disproportionates* and does not *polymerize*, once *P* and *T* are high enough to render the N–O bond heterolytic. This dominant thermal breakdown pathway is the spin-forbidden dissociation [18]



which requires a change in spin-multiplicity and therefore proceeds via electronic-state crossing across potential energy surfaces (PES) rather than on a single adiabatic PES

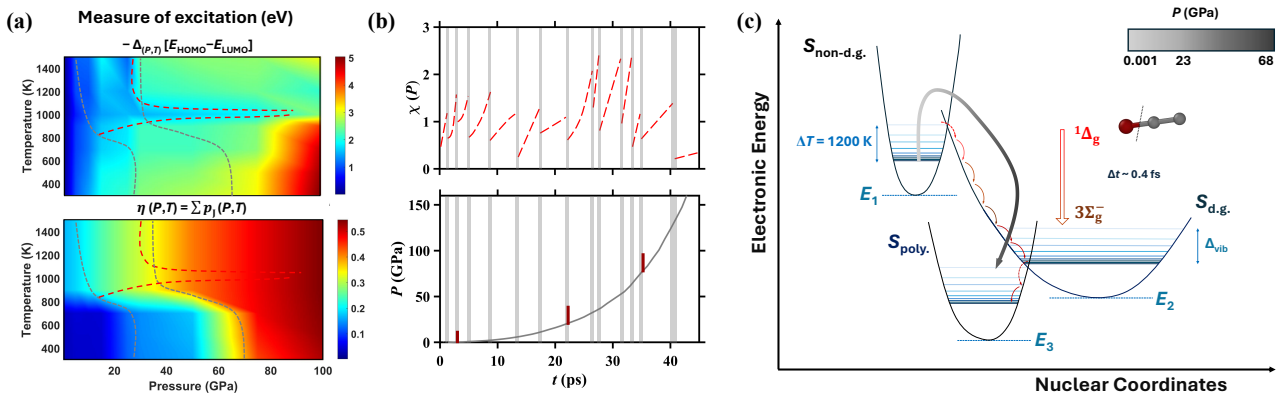


FIG. 1: General characteristics of a C-N-O system, exemplified here with data from a CO-N<sub>2</sub>O system: (a) The extent of excitation in a C-N-O system quantified as decrease in HOMO-LUMO gap as a function of pressure and temperature in the final configuration at each  $P$ - $T$  point. (b) The evolution of pressure with simulation time, along the 1200 K isotherm, highlighting in gray the specific time domains where NAMD has been performed. Red bars indicate phase transition boundaries. (c) A cartoon describing the nonadiabatic PES hopping ( $S_{\text{non-d.g.}}$  to  $S_{\text{d.g.}}$ ) as a result of singlet-oxygen dissociating from nitroxide molecules to form triplet-oxygen molecules; followed by equilibration with redistribution of energy ( $\Delta_{\text{vib}}$ ) from vibrational to translational or rotational modes to either a dissociated state ( $S_{\text{d.g.}}$ ) or a polymeric amorphous state ( $S_{\text{poly.}}$ ).

[19]. Non-adiabatic surface-hopping trajectories on high-level multireference PESs confirm that the crossing occurs at an extended region  $\sim 1.8$  Å along the N–O stretch, a geometry frequently sampled once  $P \gtrsim 1.5$  GPa and  $T \gtrsim 900$  K [20].

In CO–N<sub>2</sub>O mixtures, we can *hypothesize* that this hot and highly rovibrationally excited O(<sup>3</sup>P) fragments can further oxidize nascent CO polymers; their exothermic recombination with developing C–O frameworks oxidizing three-coordinate carbon sites to CO<sub>2</sub>. This would inject local heat, and generates point-defect disorder that frustrates any incipient crystallization, coupling unimolecular N<sub>2</sub>O decomposition to the overall amorphization chemistry. We can speculate that this might drive down the amorphization pressures; with amorphous structures being preferable over crystalline ones for the sake of recoverability [21]. Pressure-driven polymerization of CO releases on the order of 3.5–4.0 eV per monomer [13, 14], favoring network formation once intermolecular separations fall below  $\approx 3$  Å [11, 13]. Laser-pump experiments have shown that electronic excitations can lower the required pressure for network formation by  $\approx 20\%$  [11], emphasizing the role of non-adiabatic pathways even in the solid state. Thus, we can reason that the local heat released ( $\approx 1$  eV per reaction) and the spin-flip crossings along the N–O stretch can potentially act as an internal *kinetic absorbers*, driving the system towards amorphous topologies even under quasi-isothermal external conditions. Overall, the outcome can potentially be a highly heterogeneous material in which densification, NO radical-mediated oxidation, and nonadiabaticity–driven bond rearrangements occur on overlapping time scales ( $\sim 0.1$  to  $\sim 1000$  fs).

Because the N<sub>2</sub>O decomposition involves a change in

spin multiplicity, nuclei move on a *manifold* of coupled electronic states. A single adiabatic potential-energy surface cannot describe the trajectory once the system approaches the crossing. Born–Oppenheimer molecular dynamics will therefore misrepresent both the timing and energetics of bond breaking. Non-adiabatic trajectory–surface-hopping [20] or Ehrenfest dynamics [22] — explicitly including spin–orbit coupling — is required to capture the competition between mechanical work done by compression (favoring polymerization) and electronic energy released by spin-flipping N<sub>2</sub>O cleavage.

This pursuit not only unlocks findings pertaining to the high-pressure physics and chemistry of such mixtures but also demonstrates methodological limitations of using *ab initio* Born–Oppenheimer molecular dynamics in systems where oxygen atoms in nitroxides undergo a slow timescale (0.1–0.5 fs) spin-transition from singlet-to-triplet-to-singlet during the unimolecular thermal decomposition of N<sub>2</sub>O that is concurrent with pressure-induced C–N–O amorphization; a process slow enough to be comparable to the time scales of ionic motion (0.5–1.0 fs). Such a sequence/overlap of transitions under combined pressure–temperature effects, which is fundamentally nonadiabatic in nature [23] and being reported for the first time in the HED context, is the main crux of this letter.

Thus, in this letter, we combine *ab initio* Born–Oppenheimer adiabatic molecular dynamics (referred to as AIMD hereafter) with trajectory surface–hopping nonadiabatic molecular dynamics (NAMD) to survey CO–N<sub>2</sub>O mixtures, compressed from ambient pressures to 160 GPa at 300–1500 K.

All ground-state and finite-temperature calculations were performed with VASP [24–26], using projector aug-

mented wave (PAW) pseudopotentials [27] and the PBE-D3 generalized gradient approximation (GGA) exchange-correlation functional [28–30]. A plane-wave cutoff of 850 eV and a single  $(\frac{1}{4}, \frac{1}{4}, \frac{1}{4})$   $k$  point [31] sufficed for 90- and 300-atom cubic supercells. While compressing along isotherms reducing box length by 1% each step, each such  $(\rho, T)$  state was equilibrated for 5–10 ps using Born–Oppenheimer *NVT* AIMD with a Nosé–Hoover thermostat fixing temperatures along the isotherm, scalar nonadiabatic couplings were used to gauge the necessity of NAMD simulations at each  $\rho, T$  point using an in-house code [32], and if determined to be necessary, 1–1.3 ps of NAMD using the fewest switches surface hopping (FSSH) algorithm [33] and directional non-adiabatic couplings were performed, using the same in-house code to couple VASP trajectories with nonadiabatic adjustments [34]. We term this the *diabatic trajectory stitching* approach.

Much of modern high-pressure or combined-high pressure-temperature predictions for pure materials or mixtures involve AIMD, which implicitly implies Born–Oppenheimer dynamics. However, as already mentioned, analysis of CO and N<sub>2</sub>O systems which involve unimolecular dissociation of nitroxides, via a singlet-to-triplet transition of detaching oxygen atoms as it forms O<sub>2</sub> molecules, potentially requires nonadiabatic treatment. In addition, pressure itself acts as a major source of excitation, as shown in Fig. 1(a), in terms of decrease in the HOMO-LUMO gap in *P-T* space. As can be seen, the excitation can reach up to 3–5 eV for CO-N<sub>2</sub>O, which coupled with the downshift in electronic energy to a new PES upon dissociation can contribute to high levels of nonadiabaticity. In addition, the excited states population fraction  $\eta(P, t) = \sum_{J>0} p_J(P, t)$  (see SI section I for description) also shows a significant rise with combined high-*P/T* effects.

It can be estimated from classical RRKM theory [35] how much ensemble time is required for such systems to have sufficient number of gas-phase collisions to enter a reactive state and form a product completely devoid of gaseous components (See SI section II for detailed discussion). For 90–300 atom cells, ∼45 ps of combined AIMD+NAMD is sufficient for 300–1500 K simulations. We distribute the NAMD time over 11–14  $\rho, T$  points (dependent on isochore), ranging from 1–1.3 ps at each point. The rationale behind this fractional nonadiabatic treatment is the following: ionic configurational adjustments being stochastic require approximately one order of magnitude higher time to equilibrate [36] than electronic state adjustments. In essence, we present a new paradigm for analyzing systems which are metastable and susceptible to nonadiabatic electronic transitions. It presents the community with a workflow that can be used to make predictions and match experiments while being physically consistent, something a simple AIMD may not suffice for. As shown in Fig. 1(b) by gray bars, in a typical

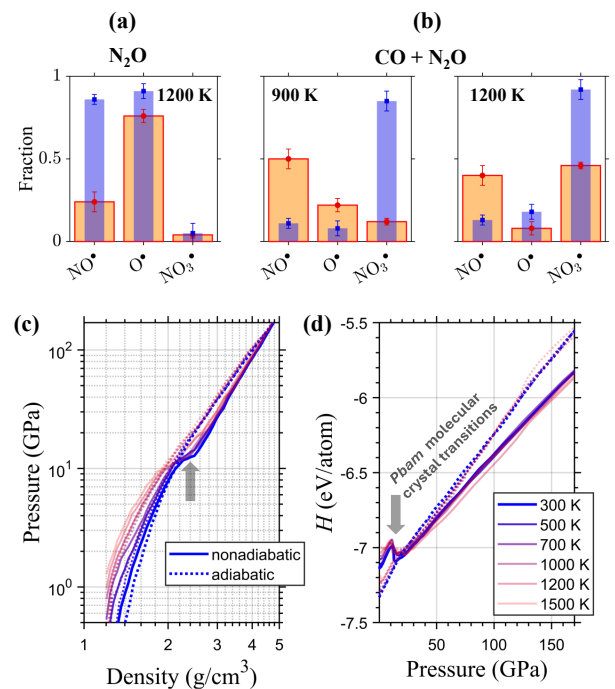


FIG. 2: Fragmentation distribution histograms for NO<sup>•</sup>, O<sup>•</sup>, and NO<sub>3</sub><sup>•</sup> free radicals in (a) N<sub>2</sub>O and (b) CO + N<sub>2</sub>O at ∼20 GPa. Black lined boxes show the fraction of N- and O-atoms in particular free radicals, whereas orange bars show the contribution of NAMD-origin free radicals to total. (c) Pressure-density equation-of-state family of curves for compression of CO<sub>2</sub> + N<sub>2</sub>O using AIMD versus NAMD simulations are shown for multiple temperatures along a heat-compress pathway. (b) Similar plots for enthalpy versus pressure are shown. In both cases, composite curves obtained from stitching together data from molecular gas, *Pbam* molecular crystal, and amorphous phases are plotted.

1200 K isothermal trajectory for CO-N<sub>2</sub>O, approximately 30.4% of the total trajectory time is used to evolve the system nonadiabatically, mostly in regions corresponding to certain transition points. When the system collapses from molecular gas to a networked solid, we can track  $\chi(P) = \eta(P, t)\gamma_e(P)$  because it couples the amount of excited population to how strongly that population shifts with pressure. Here, the electronic Grüneisen parameter  $\gamma_e(P)$  is a dimensionless measure of volume-sensitivity of an excited-state energy [37]. In CO+N<sub>2</sub>O,  $\chi$  rises from < 0.3 below 15 GPa to ≈ 2.2 at the molecular-amorphous transition pressure, providing signal for impending structural collapse.

What this type of nonadiabatic refactoring describes is shown using the energy diagram in Fig. 1(c), which shows the sequence of hopping across at least three PESs: gaseous non-dissociated ( $S_{non-d.c.}$ ) to dissociated ( $S_{d.c.}$ ) at <4 GPa; >75% fraction formation of molecular C-N-O crystal or polymeric amorphous C-N-O ( $S_{poly.}$ ) phase at ∼23 GPa and ∼68 GPa respectively. Each such hop-

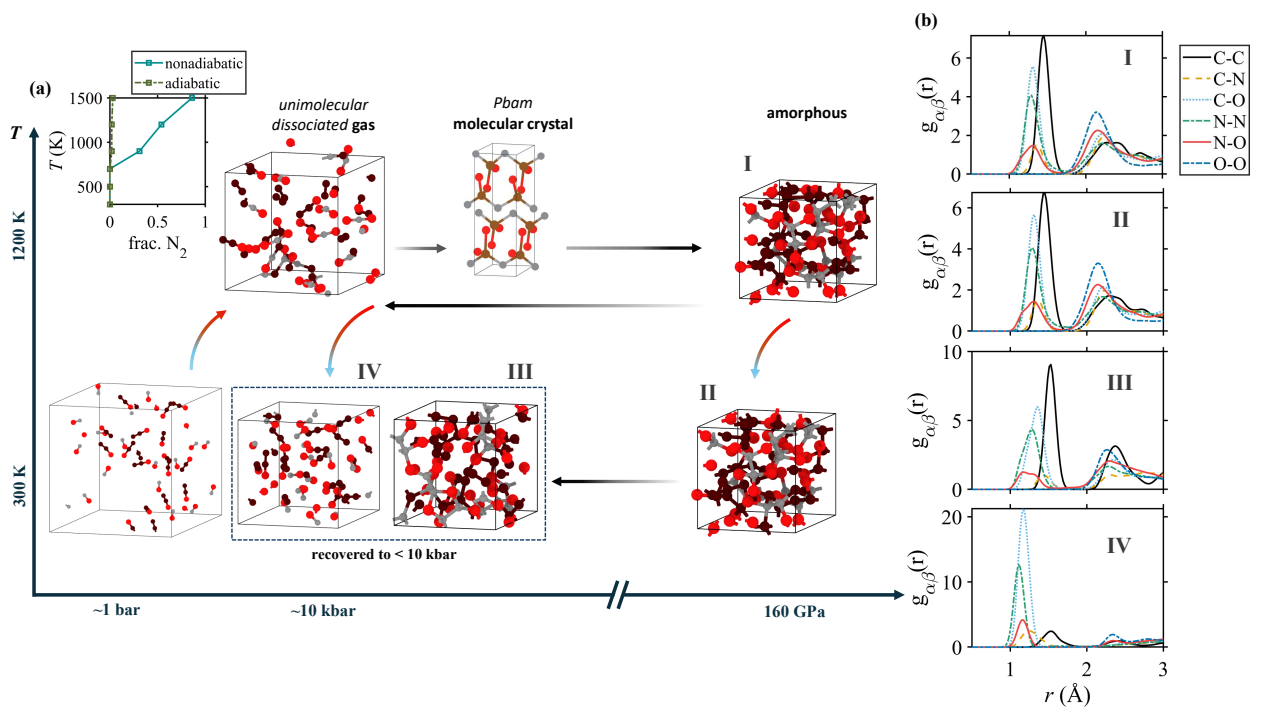


FIG. 3: (a) Formation enthalpy of different carbon monoxide-nitroxide mixtures at 160 GPa, calculated w.r.t. 1 atm constituents, as a function of temperature for the heat-compress-quench path. (b) Formation enthalpy of different carbon monoxide-nitroxide mixtures at 10 kbar, calculated w.r.t. 1 atm constituents, as a function of temperature for the heat-compress-quench-decompress path. These thermodynamic pathways are shown in the top-right corner of both (a) and (b). (c) Snapshots of different structures resulting from starting with  $CO+N_2O$  molecular gas mixtures are shown in a pressure-temperature phase diagram. The radial distribution functions of four relevant structures are shown in right-column plots, while the fractionation of  $N_2O$  to  $N_2$  is shown as a function of temperature in the inset on top-left.

ping involves a conical intersection across two PESs, and since such PESs are not continuously differentiable [38], addressing the chemical evolution of this system using machine learned interatomic potentials might lead to fictitious results. This, furthermore, makes analysis of such C-N-O systems even more challenging.

Surface-hopping NAMD trajectories exhibit hopping probabilities of up to 15 % per fs for O-transfer intermediates, with Landau-Zener coupling peaking near  $C-O = 1.85 \text{ \AA}$ . The associated non-radiative energy release heats the lattice locally by  $\sim 150 \text{ K}$  within 200 fs, accelerating further bond rearrangements — a feedback that is absent in strictly adiabatic AIMD. This reduces the onset of CO polymerization in the  $CO+N_2O$  mixtures from  $\sim 8 \text{ GPa}$  [11] in case of pure CO to  $< 5 \text{ GPa}$  in C-N-O mixtures. While this confirms one of our hypothesis, there wasn't much gain to be made anyway, in terms of reducing the polymerization-onset of CO, given the low onset pressure to begin with.

For benchmarking, we used NAMD to compare with reported data on thermalized  $N_2O$  gas. The dissociation of  $N_2O$  ( $\Sigma^+$ ) to  $N_2$  and  $O^\bullet(^3P)$  is considered to be principal case for such benchmarking, although data exists for  $NO$ ,  $NO_2$ , and  $N_2O_5$  as well [39–43]. This decomposition

is expected to be complete at 1000-1200 K at  $\sim \text{MPa}$  pressures [39]. As shown in Fig. 2(a),  $\sim 76\%$  breakdown of the  $N_2O$  molecules is achieved in the NAMD at 1200 K, with  $> 91\%$  of the contribution arising from the NAMD trajectory. The dynamics is slightly altered when CO is present in the system. In that case,  $NO^\bullet$  forms in the adiabatic trajectory unlike in the case of  $N_2O$  by itself. However, more consequential is the presence of  $\sim 46\%$   $NO_3^\bullet$  free radical at  $\sim 1200 \text{ K}$ , overwhelmingly ( $\sim 92\%$ ) originating from the NAMD trajectory. This species plays a key role in decrystallization and amorphization characteristics of C-N-O mixtures by virtue of its high reactivity [44].

The effect of the presence of this free radical can be seen in terms of changes in bulk thermodynamic variables: Fig. 2(c) shows the equation of state for the adiabatic and nonadiabatic cases at multiple temperatures, whereas Fig. 2(d) shows the same for enthalpy versus pressure. In either case, a kink is observed in the family of curves for the nonadiabatic case, irrespective of temperature, that can be attributed to not just accurately capturing the dissociation characteristics of  $N_2O$  at high temperatures, but also the  $NO_3^\bullet$  free radical at all temperatures. This correction leads to a reduction in net

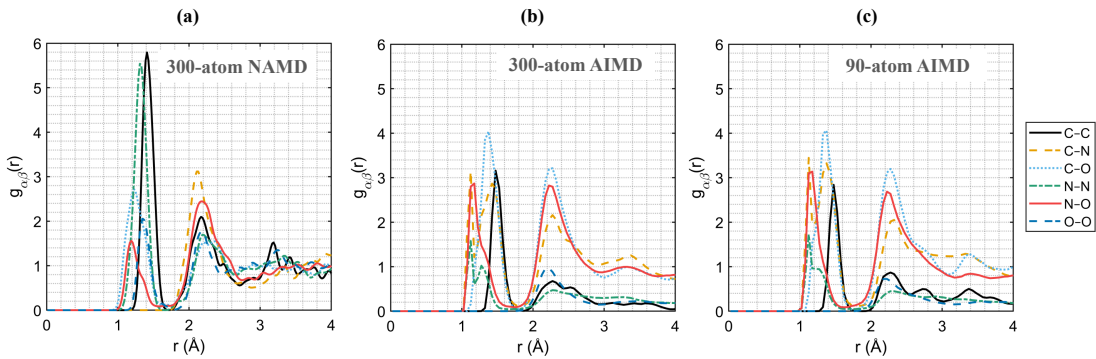


FIG. 4: Radial distribution functions of C-N-O amorphous structures formed from compression of  $\text{CO} + \text{N}_2\text{O}$  mixture along the 1200 K isotherm using (a) 300-atom nonadiabatic molecular dynamics, (b) 300-atom Born-Oppenheimer AIMD, and 90-atom Born-Oppenheimer AIMD. Comparative analysis shows drastically different second shell characteristics, alongside stronger O-O bonds, and a higher fraction of N-N bonds. This is commensurate to a lower quantity of C-N and C-O bonds.

enthalpy that can be obtained from the system. Thus, the downstream effects on added nonadiabaticity is not just altered and closer-to-reality chemical dynamics but also more accurate energetics.

At constant temperature the enthalpy is  $H(P, T) = U(P, T) + PV(P, T)$  so its pressure derivative is  $(\partial H/\partial P)_T = V - T(\partial V/\partial T)_P$ . Three contributions control the sign of  $H$ : Mechanical work  $+P dV$  – always *positive*, forcing  $H$  upward as the lattice/fluid is compressed. Thermal expansivity term  $-T(\partial V/\partial T)_P$  – negative for fluids, nearly zero for rigid amorphous solids. Chemical-bond term  $\Delta U_{\text{chem}}$  – exothermic ( $< 0$ ) when polymerization or network formation releases bond energy, endothermic ( $> 0$ ) if dissociation dominates. Below  $\sim 15$  GPa the mixture is a van-der-Waals fluid or molecular crystal, with CO amorphization; enthalpy  $H$  rises almost linearly with pressure  $P$  because only the mechanical term  $PV$  is important. Near  $P \approx 15\text{--}20$  GPa a sudden and cooperative molecular-to-amorphous-network transition *drops*  $H$ , over-compensating the  $PV$  term for a narrow window. Above  $\sim 30$  GPa the network starts becoming fully connected; its smaller molar volume means  $(\partial H/\partial P)_T$  is again positive, but with a gentler slope than in the molecular regime. If the transition were endothermic—e.g. simple dissociation into weaker bonds—no such dip would appear and  $\Delta H(P)$  would increase monotonically. Thus, from purely mechanistic/thermodynamic considerations, sigmoidal curves as in Fig. 2(c,d) nonadiabatic cases, are to be expected and these reflect a competition between *mechanical compression* (always raising the enthalpy) and *exothermic bond rearrangement* (lowering it over a limited pressure interval).

Let's examine the temperature-pressure ( $T$ - $P$ ) phase diagram of  $\text{CO} + \text{N}_2\text{O}$  mixtures for both high-pressure structures as well as for recoverability considerations. This is because synthesizing an energetic amorphous material is only a meaningful exercise if the said material can be recovered to near-ambient conditions. Beginning with

a molecular gas at roughly 1 bar, heating the system induces unimolecular dissociation above about 900 K. The inset of Fig. 3c shows that this dissociation starts at 900 K and is nearly complete by 1500 K. After dissociation, further compression produces a molecular crystal (space group  $Pbam$ ; at 25 GPa:  $a = 7.22 \text{ \AA}$ ,  $b = 3.25 \text{ \AA}$ ,  $c = 1.971 \text{ \AA}$ ,  $\alpha = 90^\circ$ ,  $\beta = 90^\circ$ ,  $\gamma = 90^\circ$ ), which, under continued compression, transforms into an amorphous structure. This molecular crystal, however, can only be obtained using constrained metadynamics. Once the compressed (160 GPa, 1200 K) amorphous structure I is attained, there are two possible pathways to attempt to recover that structure back to near-ambient conditions. The first approach (structure IV) is to decompress along the 1200 K isotherm from 160 GPa down to approximately 10 kbar, and then quench to 300 K. The second approach (structure III) is to quench first at 160 GPa from 1200 K to 300 K and subsequently decompress from 160 GPa to 10 kbar. As shown by the radial distribution functions in Fig. 3(c), the recovered structure III retains its amorphous network, whereas structure IV begins to break down into molecular constituents. We select 10 kbar as the recovery pressure because fluctuations in MD might otherwise take the system sporadically to negative pressures, which adversely affects making any physically-relevant conclusions. The recovery/decompression trajectory was simulated by increasing box length by 1% at each  $\rho, T$  point, until ensemble-averaged pressure dropped below 10 kbar. 22.6-24 ps of trajectory was simulated, with 3.6-5.2 ps using NAMD simulations, utilizing the same *diabatic trajectory stitching* approach as discussed earlier. It is very important to note here that the decompressed amorphous phase IV does not break down to molecular components when nonadiabaticity is not used in the trajectory.

It is imperative to understand the feature differences between the compressed-reactive product we get from NAMD and AIMD simulations. We pick the edge case

of  $P \approx 160$  GPa and at  $T \approx 1200$  K, and compare the features in the radial distribution function as shown in Fig. 4. Nonadiabaticity promotes enhanced dissociation of  $\text{N}_2\text{O}$  and alternate pathways to polymerization which is represented by structural differences, i.e. reduced fractions of C-N and C-O bonds, stronger O-O bonds and higher fraction of N-N bonds. The accurate simulation of  $\text{N}_2\text{O}$  disproportionation introduces highly reactive NO and O free radicals which assists in enhanced formation of O-O and N-N bonds.

This letter underscores the need for combining nonadiabatic calculations with Born-Oppenheimer molecular dynamics to capture the complex phase behavior of reactive C-N-O mixtures under pressure. We find that the dissociation and the nature of amorphization are driven by pressure-enhanced  $\text{N}_2\text{O}$  decomposition, with structural signatures imprinted in enthalpy and recoverability characteristics. Recoverability of high-pressure phases is sensitive to the path taken, emphasizing the role of local energy metrics in high-pressure physics and chemistry.

This work was performed under the auspices of the U.S. Department of Energy by Lawrence Livermore National Laboratory (LLNL) under contract number DEAC52-07NA27344. The authors acknowledge funding support from the DOE Laboratory Directed Research and Development (LDRD) program at LLNL under the project tracking code 23-ER-028. We would like to thank Livermore Computing (LC) for helping us in finishing this extremely expensive study by utilizing  $\sim 28$  million cpu-hours.

---

[1] S. G. Zlotin, A. M. Churakov, M. P. Egorov, L. L. Fershtat, M. S. Klenov, I. V. Kuchurov, N. N. Makhova, G. A. Smirnov, Y. V. Tomilov, and V. A. Tartakovskiy, *Mendeleev Communications* **31**, 731 (2021).  
[2] E. R. Bernstein, *Advances in quantum chemistry* **69**, 31 (2014).  
[3] J. T. Clemmer, K. N. Long, and J. A. Brown, *Mechanics of Materials* **184**, 104693 (2023).  
[4] M. I. Eremets, I. A. Trojan, A. G. Gavriliuk, and S. A. Medvedev, *Static Compression of Energetic Materials* , 75 (2008).  
[5] M. J. Lipp, W. J. Evans, B. J. Baer, and C.-S. Yoo, *Nature materials* **4**, 211 (2005).  
[6] S. Bonev, M. Lipp, J. Crowhurst, and J. McCarrick, *The Journal of Chemical Physics* **155** (2021).  
[7] M. A. Kettner and T. M. Klapötke, in *Chemical rocket propulsion: A comprehensive survey of energetic materials* (Springer, 2016) pp. 63–88.  
[8] X. Yong, H. Liu, M. Wu, Y. Yao, J. S. Tse, R. Dias, and C.-S. Yoo, *Proceedings of the National Academy of Sciences* **113**, 11110 (2016).  
[9] H. Yurtseven, Ö. Tiryaki, and O. Tari, *Anadolu University Journal of Science and Technology A-Applied Sciences and Engineering* **17**, 741 (2016).  
[10] F. Datchi, M. Moog, F. Pietrucci, and A. M. Saitta, Pro-

ceedings of the National Academy of Sciences **114**, E656 (2017).  
[11] W. J. Evans, M. J. Lipp, C.-S. Yoo, H. Cynn, J. L. Herberg, R. S. Maxwell, and M. F. Nicol, *Chemistry of Materials* **18**, 2520 (2006).  
[12] W. J. Evans, M. J. Lipp, C.-S. Yoo, H. Cynn, J. L. Herberg, R. S. Maxwell, and M. F. Nicol, *Pressure-Induced Polymerization of Carbon Monoxide: Disproportionation and Synthesis of an Energetic Lactonic Polymer*, Tech. Rep. UCRL-TR-216925 (Lawrence Livermore National Laboratory, Livermore, CA, 2005).  
[13] K. Xia, J. Sun, C. J. Pickard, D. D. Klug, and R. J. Needs, *Physical Review B* **95**, 144102 (2017).  
[14] C.-L. Sun, Q. Liu, H. Wang, T. Cui, and Y. Ma, *Physical Review B* **104**, 094102 (2021).  
[15] R. L. Mills, B. Olinger, D. T. Cromer, and R. LeSar, *The Journal of Chemical Physics* **95**, 5392 (1991).  
[16] V. Iota, C. Park, and C.-S. Yoo, *Physical Review B* **69**, 064106 (2004).  
[17] C.-S. Yoo, A. Sengupta, M. Kim, G. Shen, B. Maddox, V. Iota, and M. F. Nicol, *The Journal of Physical Chemistry B* **107**, 5922 (2003).  
[18] G. Herzberg, *Molecular Spectra and Molecular Structure, Vol. I: Spectra of Diatomic Molecules*, 2nd ed. (Van Nostrand, New York, 1950).  
[19] D.-Y. Hwang and A. M. Mebel, *Chemical Physics* **255**, 169 (2000).  
[20] J. E. Subotnik, A. Jain, B. Landry, A. S. Petit, W. Ouyang, N. Bellonzi, and P. Zimmerman, *Annual Review of Physical Chemistry* **67**, 387 (2016).  
[21] M. Santoro, F. A. Gorelli, R. Bini, G. Ruocco, S. Scandolo, and W. A. Crichton, *Nature* **441**, 857 (2006).  
[22] B. F. E. Curchod and T. J. Martínez, *Chemical Reviews* **118**, 3305 (2018).  
[23] A. Bhattacharya, Y. Guo, and E. R. Bernstein, *Accounts of chemical research* **43**, 1476 (2010).  
[24] G. Kresse and J. Hafner, *Physical Review B* **47**, 558 (1993).  
[25] G. Kresse and J. Furthmüller, *Computational Materials Science* **6**, 15 (1996).  
[26] G. Kresse and J. Furthmüller, *Physical Review B* **54**, 11169 (1996).  
[27] P. E. Blöchl, *Physical Review B* **50**, 17953 (1994).  
[28] J. P. Perdew, K. Burke, and M. Ernzerhof, *Physical Review Letters* **77**, 3865 (1996).  
[29] J. P. Perdew, J. A. Chevary, S. H. Vosko, K. A. Jackson, M. R. Pederson, D. J. Singh, and C. Fiolhais, *Physical Review B* **46**, 6671 (1992).  
[30] A. D. Becke, *The Journal of Chemical Physics* **96**, 2155 (1992).  
[31] A. Baldereschi, *Physical Review B* **7**, 5212 (1973).  
[32] W. Chu, J. Zheng, S. A. Pshenichnyuk, S. Tretiak, and A. I. Krylov, *The Journal of Physical Chemistry Letters* **12**, 760 (2021).  
[33] J. C. Tully, *The Journal of Chemical Physics* **93**, 1061 (1990).  
[34] A. V. Akimov and O. V. Prezhdo, *Journal of Chemical Theory and Computation* **9**, 4959 (2013).  
[35] J. L. Magee, *Proceedings of the National Academy of Sciences* **38**, 764 (1952).  
[36] B. F. Curchod and T. J. Martínez, *Chemical reviews* **118**, 3305 (2018).  
[37] P. Y. Yu and M. Cardona, *Fundamentals of Semiconductors: Physics and Materials Properties*, 4th ed. (Springer,

Berlin Heidelberg, 2010).

- [38] D. R. Yarkony, *Reviews of Modern Physics* **68**, 985 (1996).
- [39] H. Loirat, F. Caralp, W. Forst, and C. Schoenenberger, *The Journal of Physical Chemistry* **89**, 4586 (1985).
- [40] G. Papapolymerou and L. D. Schmidt, *Langmuir* **1**, 488 (1985).
- [41] A. Karabeyoglu, J. Dyer, J. Stevens, and B. Cantwell, in *44th AIAA/ASME/SAE/ASEE Joint Propulsion Conference & Exhibit* (2008) p. 4933.
- [42] E. K. Gill and K. J. Laidler, *Canadian Journal of Chemistry* **36**, 1570 (1958).
- [43] H. Johnston, C. Cantrell, and J. Calvert, *Journal of Geophysical Research: Atmospheres* **91**, 5159 (1986).
- [44] F. Karagulian and M. J. Rossi, *The Journal of Physical Chemistry A* **111**, 1914 (2007).

## SUPPLEMENTARY INFORMATION

### I. EXCITED STATES POPULATION FRACTION

$$\eta(P, t) = \sum_{J>0} p_J(P, t).$$

Here,  $\eta(P, t)$  is the excited-state population fraction (dimensionless,  $0 \leq \eta \leq 1$ ) at external parameter  $P$  (in this context, pressure) and time  $t$ .  $J$  is the index of adiabatic electronic states ordered by energy;  $J = 0$  is the ground state,  $J > 0$  are excited states. The sum runs over all excited states.  $p_J(P, t)$  is the population (probability) of being on electronic state  $J$  at  $(P, t)$ .

In practice, when using FSSH/NA-MD based on electronic coefficients,  $P_J = \langle |c_J(t)|^2 \rangle_{\text{traj}}$  and when active-surface occupancy is used:  $P_J = \frac{1}{N_{\text{traj}}} \sum_k \mathbf{1}[J_k^{\text{active}}(t) = J]$ .

Normalization:  $\sum_{J \geq 0} P_J(P, t) = 1$ , so equivalently  $\eta(P, t) = 1 - P_0(P, t)$ .

Notes: If states have degeneracy  $\mathbf{g}_J$ , either treat each component as a separate  $J$  in the sum or weight by  $g_J$ . If the basis is truncated, ensure populations are renormalized so the total remains 1.

### II. RRKM/NA-TST TIMES OF FIRST-EVENT TIMES FOR CO + N<sub>2</sub>O MIXTURES

We estimate the *waiting time to the first reactive event* that seeds amorphization during isothermal compression of mixed CO + N<sub>2</sub>O, using RRKM/statistical kinetics augmented by nonadiabatic transition-state theory (NA-TST). The objective is a predictive, box-size-dependent criterion showing what time limit of *ab initio*/nonadiabatic molecular dynamics is *sufficient* to observe the onset of chemistry for both **90-atom** and **300-atom** cells over 300 K to 1500 K. We provide closed-form scaling, a Landau-Zener nonadiabatic factor, and tabulated median ( $t_{50}$ ) and conservative ( $t_{95}$ ) first-event times.

#### Calculate Reactive Rate Constants for Gas-amorphous transition

##### Per-encounter *gas-like* capture Model

We adopt a capture-complex-branching picture for short-range CO · · · N<sub>2</sub>O encounters. The effective *bimolecular* reactive rate constant is

$$k_2(T) = \langle \sigma v \rangle_T P_{\text{react}}(T, P), \quad (1)$$

where  $\langle \sigma v \rangle_T$  is the kinetic capture factor and  $P_{\text{react}}$  is the *per-encounter* success probability (RRKM branching within the energized complex multiplied by a nonadiabatic hop probability). For hard-sphere kinetics

$$\sigma = \pi \left( \frac{d_{\text{CO}} + d_{\text{N}_2\text{O}}}{2} \right)^2, \quad (2)$$

$$\langle v \rangle = \sqrt{\frac{8k_{\text{B}}T}{\pi\mu}}, \quad \text{and} \quad (3)$$

$$\mu = \frac{m_{\text{CO}} m_{\text{N}_2\text{O}}}{m_{\text{CO}} + m_{\text{N}_2\text{O}}}. \quad (4)$$

We use kinetic diameters  $d_{\text{CO}} = 3.76 \text{ \AA}$  and  $d_{\text{N}_2\text{O}} = 3.30 \text{ \AA}$  [1, 2].

For the energized collision complex, the RRKM micro-canonical branching ratio for product formation is

$$\begin{aligned} p_{\text{prod}}(E) &= \frac{k_{\text{prod}}(E)}{k_{\text{prod}}(E) + k_{\text{back}}(E)} \\ &= \frac{N_{\text{prod}}^{\ddagger}(E - E_0)}{N_{\text{prod}}^{\ddagger}(E - E_0) + N_{\text{back}}^{\ddagger}(E - E_0)} \end{aligned} \quad (5)$$

with standard densities/counts of states. A necessary hop at a diabatic crossing has the Landau-Zener probability[3]

$$P_{\text{LZ}}(E) = 1 - \exp \left[ -\frac{2\pi H_{ab}^2}{\hbar v_{\perp}(E) |\Delta F|} \right], \quad (6)$$

where  $H_{ab}$  is the electronic coupling,  $\Delta F$  the diabatic slope difference, and  $v_{\perp}$  the normal velocity through the crossing. Canonically averaged,

$$P_{\text{react}}(T, P) = \langle p_{\text{prod}}(E) P_{\text{LZ}}(E) \rangle_T, \quad (7)$$

which is the NA-TST extension of RRKM for spin-crossing or electronically nonadiabatic channels [4].

*Waiting-time statistics in a periodic box.* For equimolar CO and N<sub>2</sub>O counts,  $N_A = N_B$  in a box of volume  $V$ , the Poisson propensity for the *first* A+B reaction is

$$\lambda = k_2(T) \frac{N_A N_B}{V}, \quad (8)$$

which yields exponential order statistics:  $t_{50} = \ln 2/\lambda$  and  $t_{95} = \ln 20/\lambda$ .

*Useful scaling.* At fixed  $k_2$ ,  $t \propto V/(N_A N_B)$ ; at fixed number density (i.e.  $V \propto N_A + N_B$  for equimolar boxes),  $t \propto 1/N$ ; and at fixed composition  $t \propto 1/(\sigma\sqrt{T} P_{\text{react}})$  via Eq. (4). These relations are used below to compare 90- and 300-atom boxes and to rescale along isotherms during compression.

### Per-attempt solid-like Eyring Model

In highly compressed, nearly amorphous environments, “collisions” blur into repeated barrier-crossing *attempts* with Eyring frequency  $\nu = k_B T/h$ . The per-site rate is  $k_{\text{site}} = P_{\text{attempt}} \nu$ , and the box-level first-event time for  $N_{\text{mol}}$  statistically independent sites is

$$t_p = \frac{-\ln(1-p)}{N_{\text{mol}} P_{\text{attempt}} k_B T/h}. \quad (9)$$

This variant leads to the same linear-in- $N$  acceleration as the previous model and is convenient when  $P_{\text{attempt}}$  is read off directly from nonadiabatic MD (NAMD).

### Parameters, geometry, and compression

We consider equimolar boxes of:

- **90 atoms:**  $N_{\text{CO}} = 18$ ,  $N_{\text{N}_2\text{O}} = 18$  ( $N_{\text{mol}} = 36$ ).
- **300 atoms:**  $N_{\text{CO}} = 60$ ,  $N_{\text{N}_2\text{O}} = 60$  ( $N_{\text{mol}} = 120$ ).

At ambient pressure, the **300-atom** box has side  $L = 21.4 \text{ \AA}$  ( $V = 9.80 \times 10^{-27} \text{ m}^3$ ). Along isotherms to  $\sim 160 \text{ GPa}$ , the box length decreases by  $\sim 34\%$ , so  $V/V_0 \approx 0.287$ . Times below are given at ambient volume and, in parentheses, multiplied by 0.287 as a conservative compressed-volume proxy.

### Calibration to NAMD: checking for 45-ps sufficiency

NAMD/AIMD show that **45 ps suffices** to observe the onset of chemistry even in the **90-atom** box. Two equivalent calibrations reconcile the statistical model with this:

(A) *Per-encounter calibration (Capture model).* Solving  $t_{50}(90 \text{ atoms}, 300 \text{ K}) = 45 \text{ ps}$  for Eq. (1)–(4) gives an effective

$$P_{\text{react}} \approx 6 \times 10^{-4} \quad (0.06\%).$$

By linear-in- $N$  scaling, the **300-atom** box requires only  $\sim 1.76 \times 10^{-4}$  (0.0176%) for the same  $t_{50}$  at 300 K, and less at higher  $T$ .

(B) *Per-attempt calibration (Eyring picture).* With  $\nu = k_B T/h$ , Eq. (9) yields  $P_{\text{attempt}} \approx 6.8 \times 10^{-5}$  at 300 K (and  $\approx 1.37 \times 10^{-5}$  at 1500 K) to achieve  $t_{50} = 45 \text{ ps}$  for the 90-atom box. These values lie in the common  $10^{-5}$ – $10^{-4}$  band for condensed-phase ( $> \text{MPa}$ ), nonadiabatic channels [3, 4].

Both are consistent with the well-established pressure-enabled reactivity and polymerization/disproportionation of CO at modest GPa even near room temperature, which accelerates further at higher  $P$  and  $T$  [5, 6].

We adopt a single *floor* value  $X \equiv 100 \times P_{\text{react}} = 0.10\%$  (compatible with meV-scale Landau–Zener couplings and rare-event crossings per close approach of PESs). With this  $X$ , both boxes comfortably meet the 45 ps criterion across 300 K to 1500 K; compression of boxes only shortens the times.

### Median first-event time $t_{50}$ (ps) at $X = 0.10\%$

Numbers outside/inside parentheses correspond to ambient volume and compressed volume ( $\times 0.287$ ), respectively.

TABLE I:  $t_{50}$  (ps) vs.  $T$  at  $X = 0.10\%$ .

$T$ (K)	90 atoms	300 atoms
300	26.37 (7.57)	7.91 (2.27)
500	20.43 (5.86)	6.13 (1.76)
700	17.26 (4.95)	5.18 (1.49)
900	15.23 (4.37)	4.57 (1.31)
1200	13.19 (3.79)	3.96 (1.14)
1500	11.79 (3.39)	3.54 (1.02)

### Conservative $t_{95}$ (ps) at $X = 0.10\%$

We use  $t_{95} = 4.322 t_{50}$  from exponential order statistics.

TABLE II:  $t_{95}$  (ps) vs.  $T$  at  $X = 0.10\%$ .

$T$ (K)	90 atoms	300 atoms
300	113.98 (32.71)	34.19 (9.81)
500	88.29 (25.34)	26.49 (7.60)
700	74.62 (21.42)	22.38 (6.42)
900	65.84 (18.90)	19.74 (5.66)
1200	56.95 (16.35)	17.09 (4.91)
1500	50.99 (14.64)	15.29 (4.39)

*Interpretation.* At ambient density,  $t_{50}$  is  $\ll 45 \text{ ps}$  for both boxes across 300 K to 1500 K; under compression ( $V/V_0 \approx 0.287$ ), even  $t_{95}$  falls below 45 ps. If one wishes to reproduce exactly  $t_{50} \approx 45 \text{ ps}$  at 300 K in the **90-atom** box at ambient density, setting  $X = 0.06\%$  achieves this; the same  $X$  gives  $t_{50} \approx 12.6 \text{ ps}$  and  $t_{95} \approx 54.6 \text{ ps}$  upon compression, again making 45 ps a safe window.

### Dilute gas-phase baseline

For dilute-gas (ambient pressure), single-pulse shock-tube and infrared-emission studies of the *direct* exchange channel  $\text{CO} + \text{N}_2\text{O} \rightarrow \text{CO}_2 + \text{N}_2$  over  $\sim 1100 \text{ K}$  to  $2300 \text{ K}$  report Arrhenius rate constants that, when compared to

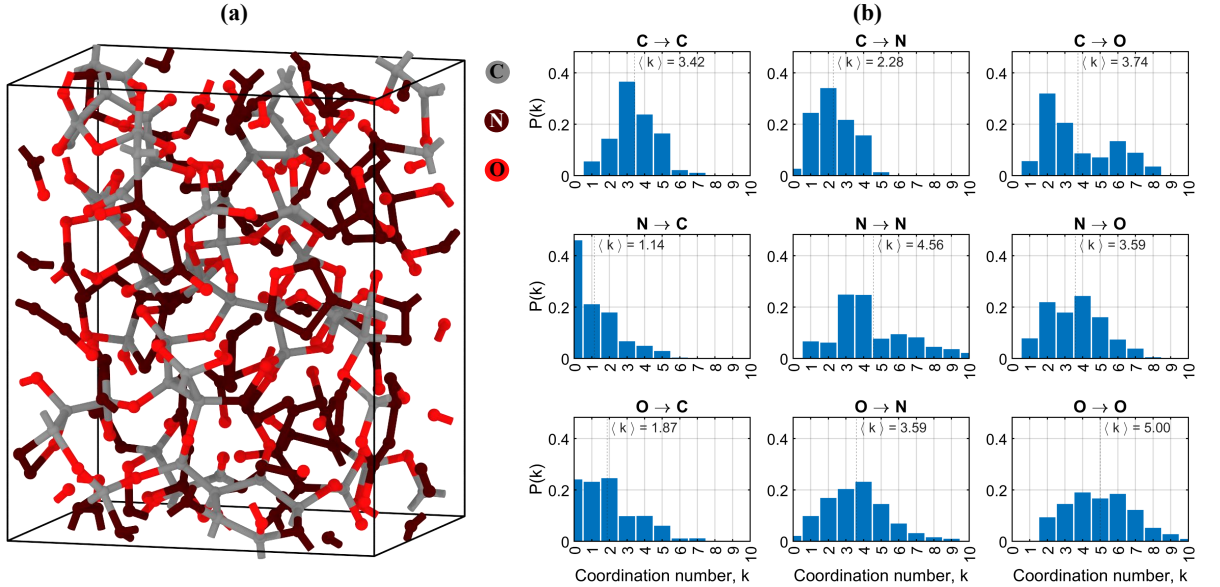


FIG. S1: (a) 300-atom final snapshot structure of amorphous C-N-O product, obtained at 160 GPa and 1200 K, and (b) nearest neighbor coordination number (NNCN) histograms of this configuration.

$\langle\sigma v\rangle$ , imply per-encounter probabilities  $\ll 10^{-3}\%$  even near 1500 K [7–9]. Such values are far too small to explain picosecond-scale initiation in dense, compressed cells. By contrast, carbon monoxide is known to react/polymerize at ps-scales readily above a few GPa (even near room temperature) in the solid/condensed environment,[5, 6] justifying an *effective*  $X$  in the  $10^{-4}$ – $10^{-3}$  range (and higher as compression proceeds), consistent with the values above. Thus, a 45-ps NAMD/AIMD might overpredict the transition pressure of amorphization because of inadequate simulations frames in the dilute-gas limit but at  $>$ MPa pressures, it should be accurate.

### Conclusions

For any alternative stoichiometry or density path, we use

$$t_{50} = \frac{\ln 2}{k_2} \frac{V}{N_A N_B}, \quad k_2 = \langle\sigma v\rangle X/100,$$

with Eqs. (4). Time scales linearly with  $V$  at fixed  $X$  and  $T$ , and inversely with  $N_A N_B$ .

With a floor  $X = 0.10\%$ , both **90-atom** and **300-atom** CO+N<sub>2</sub>O boxes exhibit median first-event times well below 45 ps across 300 K to 1500 K, and  $t_{95} < 45$  ps upon compression to  $\sim$ 160 GPa.

### III. GENERAL DOMAIN OF PRESSURE-INDUCED DISSOCIATION AND POLYMERIZATION

#### Breakdown of the Born–Oppenheimer picture under compression

We assess where nonadiabatic molecular dynamics (NA-MD) is required along the CO + N<sub>2</sub>O compression path (0–200 GPa) using two yardsticks: the Landau–Zener adiabaticity parameter  $\gamma$  and the electron–phonon thermalization time  $\tau_{e-ph}$  relative to a characteristic nuclear period  $\tau_n$ .

$$\gamma = \frac{\hbar}{E_{eg}^2} \left| \dot{\mathbf{R}} \cdot \left\langle \Psi_e \left| \frac{\partial H}{\partial \mathbf{R}} \right| \Psi_g \right\rangle \right|, \quad (10)$$

where  $E_{eg}$  is the instantaneous adiabatic energy gap between the ground ( $\Psi_g$ ) and an excited ( $\Psi_e$ ) electronic state,  $\mathbf{R}$  are nuclear coordinates, and  $\dot{\mathbf{R}}$  their velocities. *Rule of thumb* – Consider also the ratio of the electronic thermalization time  $\tau_{e-ph}$  to a characteristic nuclear period  $\tau_n$  ( $\approx 100$  fs for the high-frequency CO stretch). When either  $\gamma \gtrsim 0.1$  or  $\tau_{e-ph} \lesssim \tau_n$ , you must step beyond ground-state Born–Oppenheimer MD.

In practice, BO descriptions remain reliable for equilibrium structure and coarse thermodynamics up to  $\sim$ 60 GPa, but specific events (spin crossover; conical-intersection bond exchanges) already require nonadiabatic treatment in the 6–30 GPa window. Once the band gap collapses near  $\sim$ 90 GPa, electrons cannot follow the nuclei adiabatically anywhere in the cell, and

TABLE S1: Pressure-resolved guidance for when nonadiabatic MD is needed during  $\text{CO} + \text{N}_2\text{O}$  compression.

P range (GPa)	Dominant physics	$E_g$ (eV)	$\tau_{e-ph}$ (fs)	Need NAMD?	Suggested method
0–4	Cold molecular fluid	7–8	> 5000	No (BO okay)	BO-AIMD / reactive FF
4–15	Spin-forbidden $\text{N}_2\text{O}$ cleavage $\rightarrow \text{CO}_2 + \text{N}_2$ (local crossings)	6–7	3000–5000	Yes (local) at crossings	Surface hopping + SOC (ps windows)
15–20	Exothermic onset; first poly-CO / poly- $\text{N}_2\text{O}$ links	4–6	1000–2000	Mostly BO; Nonadiabaticity for chain-growth events	SH/SHARC on reactive trajectories
20–65	C–N–O framework growth; shrinking gap	2–3	300–800	Borderline (Nonadiabaticity for energy-flow studies)	Ehrenfest/SHARC on subsets
65–100	Insulator $\rightarrow$ semiconductor crossover	0.5–2	50–300	Growing nonadiabaticity ( $\text{P} dV$ work)	Ehrenfest-TDDFT / two-temperature AIMD
~90	Band-gap collapse / incipient metallization	$\lesssim 0.4$	10–50	System-wide BO breakdown	Decoherence-corrected Ehrenfest / NEAIMD
100–160	Metallic C–N–O alloy (degenerate electrons)	0	5–20	NAMD mandatory	Two-temperature NA-AIMD / MDEF-TDDFT

fully nonadiabatic dynamics become necessary through the 100–200 GPa metallic regime.

#### IV. TRAJECTORY IN *NVE* NAMD/AIMD SIMULATIONS

Starting from the initial 300-atom configuration at ambient pressure and room temperature, each *NVE* point is obtained by a geometric volume update (1% side length reduction each step) enforcing unique densities and a final  $\rho = 4.56 \text{ g cm}^{-3}$  at 156.2 GPa over a simulation duration of  $\sim 52.0 \text{ ps}$  ( $\sim 8.8 \text{ ps}$  in NAMD). Thermal evolution is adiabatic within piecewise regimes, with small latent releases near transitions; a localized thermal spike is seen in the 10–20 GPa window indicative of exothermic reaction. We report  $H/H_0 = (U + PV)/H_0$  (with  $H_0$  the ambient enthalpy), constrained to start at 1 and rises to 3.56 at 156.2 GPa.

*Regime I:* 0–4 GPa (condensed gaseous/molecular).  $T(P)$  nearly flat;  $\rho(P)$  increases smoothly;  $H/H_0$  rises rapidly from 1 due to  $PV$  work with minimal chemistry. *Regime II:* 4–15 GPa (onset of chemistry). Gentle heating; first kink in  $T(P)$  and  $H/H_0(P)$ ;  $\rho(P)$  remains monotone.

*Regime III:* 15–20 GPa (polymerization/lock-in). Signature triad is observed: (i) a *dip* in  $H/H_0(P)$  indicating net stabilization, (ii) a *plateau* (very flat to slightly negative slope) in  $\rho(P)$  over 15.2–19.6 GPa, and (iii) a *local spike* in  $T(P)$  consistent with exothermic bond reconfig-

uration.

*Regime IV:* 20–65 GPa (framework growth).  $H/H_0$  resumes a positive slope but smaller than pre-dip;  $T(P)$  increases with reduced slope as the network thickens;  $\rho(P)$  recovers to a smooth rise.

*Regime V:* 65–100 GPa (gap-shrinking/ionic contribution). Continued densification; modest kinks in  $T(P)$  and  $H/H_0(P)$ .

*Regime VI:* 100–156 GPa (deep densification). Smooth approach to the final constraints ( $\rho = 4.56 \text{ g cm}^{-3}$ ,  $T = 1685 \text{ K}$ ,  $H/H_0 \simeq 3.56$ ).

As can be seen in Fig. S1(a),  $T(P)$  rises stepwise with a localized spike in the 10 GPa to 20 GPa window, signaling the onset of network-forming chemistry. Fig. S1(b) shows  $T$  against  $\rho$  recasts the same thermal excursion at  $\rho \approx 1.8 \text{ g cm}^{-3}$  to  $2.1 \text{ g cm}^{-3}$  while preserving the strictly monotonic compression path. Fig. S1(c) shows the mechanical response,  $\rho(P)$ , exhibits a pronounced plateau—with near-zero to slightly negative slope—between 10.2 GPa and 19.6 GPa, followed by a smooth recovery into a stiffer densification regime above 20 GPa. Fig. S1(d) shows the energetics,  $H/H_0(P)$  shows a shallow dip over 10 GPa to 20 GPa and then a gradual rebound to  $\approx 3.56$  by 156 GPa, with a reduced post-event slope relative to the pre-event segment. Taken together, Fig. S1(a)–(d) trace a coherent sequence: molecular condensation  $\rightarrow$  exothermic, nonadiabatic bond reconfiguration (dip/plateau/spike triad)  $\rightarrow$  framework growth and progressive densification.

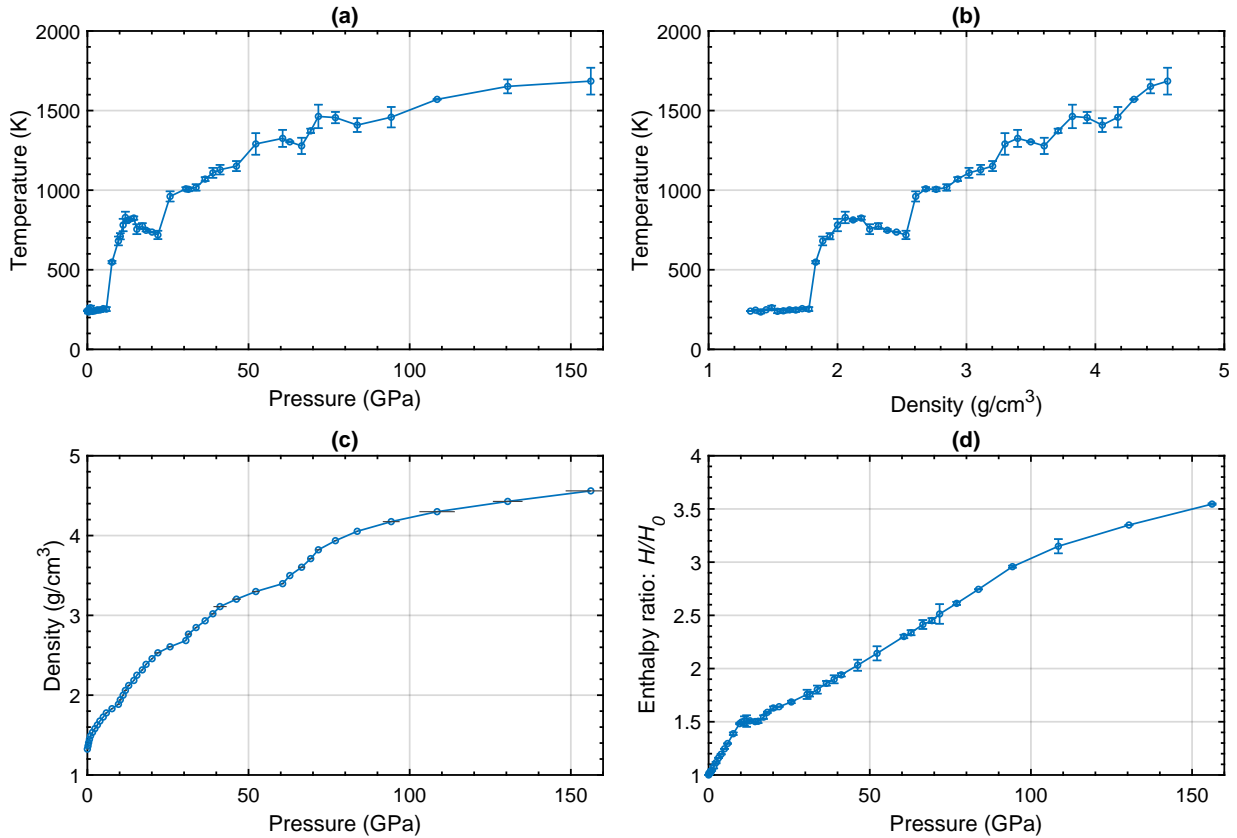


FIG. S2: Equation of state data from *NVE* trajectory simulations: (a) temperature versus pressure, (b) temperature versus density, (c) density versus pressure, and (d) enthalpy ratio relative to ambient enthalpy versus pressure.

---

[1] D. W. Breck, *Zeolite Molecular Sieves: Structure, Chemistry, and Use* (Wiley, New York, 1974).

[2] S. Matteucci, Y. Yampolskii, B. D. Freeman, and I. Pinnau, *Materials Science of Membranes for Gas and Vapor Separation* (Wiley, Chichester, 2006), Ch. 1.

[3] C. Wittig, The Landau-Zener Formula, *J. Phys. Chem. B* **109**, 8428–8430 (2005).

[4] A. O. Lykhin and S. A. Varganov, Nonadiabatic Transition State Theory: Application to Intersystem Crossings in the Active Sites of Metal-Sulfur Proteins, *Int. J. Quantum Chem.* **116**, 750–761 (2016).

[5] W. J. Evans, M. A. Morales, M. C. Martin, *et al.*, Pressure-Induced Polymerization of Carbon Monoxide, *Chem. Mater.* **18**, 2520–2531 (2006).

[6] W. J. Evans, L. Fagundo, P. Y. Zavalij, *et al.*, *Pressure-*

*Induced Polymerization of Carbon Monoxide: Disproportionation and Synthesis of an Energetic Lactonic Polymer*, U.S. DOE OSTI Report 884767 (2005).

[7] M. C. Lin and S. H. Bauer, Bimolecular Reaction of  $\text{N}_2\text{O}$  with CO and the Recombination of O and CO as Studied in a Single-Pulse Shock Tube, *J. Chem. Phys.* **50**, 3377–3391 (1969).

[8] N. Fujii, T. Kakuda, T. Sugiyama, and H. Miyama, Direct Determination of the Rate Constant for the Reaction  $\text{CO} + \text{N}_2\text{O} \rightarrow \text{CO}_2 + \text{N}_2$ , *Chem. Phys. Lett.* **122**, 489–492 (1985).

[9] H. Loirat, F. Caralp, M. Destriau, and R. Lesclaux, Oxidation of Carbon Monoxide by Nitrous Oxide between 1076 and 1228 K: Determination of the Rate Constant of the Exchange Reaction, *J. Phys. Chem.* **91**, 6538–6542 (1987).